

MoO₃ Structures Transition from Nanoflowers to Nanorods and Their Sensing Performances

Li-Bin Hu

Qingdao University

Xin-Yu Huang

Qingdao University

Shan Zhang

Qingdao University

Xue Chen

Engineering Research Center for Semiconductor Integrated Technology, Institute of Semiconductors, Chinese Academy of Sciences, Beijing 100083, China

Xian-Hui Dong

Qingdao University

He Jin

Qingdao University

Zhen-Yu Jiang

Qingdao University

Xiao-Ran Gong

Qingdao University

Yi-Xuan Xie

Qingdao University

Chen Li

Qingdao University

Zong-Tao Chi

Qingdao University

Wan-Feng Xie (✉ wfxie@qdu.edu.cn)

Qingdao University <https://orcid.org/0000-0002-5477-7988>

Research Article

Keywords: MoO₃, annealing temperature, morphology, crystallization, ethanol sensing performance

Posted Date: March 12th, 2021

DOI: <https://doi.org/10.21203/rs.3.rs-283514/v1>

License:  This work is licensed under a Creative Commons Attribution 4.0 International License.

[Read Full License](#)

Abstract

Morphology transformation and crystal growth strategies of metal oxide semiconductors are extensively studied in material science recently, because the morphology and crystallinity of the nanomaterial have significant effects on the physicochemical characteristics. However, understanding the morphology changes of α - MoO_3 induced by annealing temperature is still a challenge. Herein, the nanostructure transition of MoO_3 induced by calcined temperature has been investigated through XRD and SEM methods. It can be found that crystallization is highly dependent on the annealing temperature. In addition, the MoO_3 nanoflowers can change into nanosheets at 500 °C. Afterwards, the nanosheets turn into microrods, especially at 900 °C due to the growth of MoO_3 crystal. On the other hand, MoO_3 is a traditional sensing material, which is sensitive to many volatile organic compounds. Thus, the sensing performances of various MoO_3 nanostructures were measured. Compared with MoO_3 nanoflowers and microrods, the MoO_3 nanosheets-based sensor has excellent sensing performance towards ethanol, and the maximum gas response value is 8.06.

1. Introduction

In the past few decades, the development of nanotechnology and band gap engineering have created various exotic metal oxide semiconductor (MOS) nanostructures, which open up new perspectives for their exploitation, significantly creating novel and fascinating devices [1–5]. Consequently, metal oxide semiconductors have attracted significant attention in recent years for their applications to secondary cells, sensors, memories, photodetectors, field-effect transistors, and heavy metal etc. [6–12]. For example, the traditional semiconductors of MoO_3 [13], In_2O_3 [14], TiO_2 [15] and ZnO [16], owing to their useful features such as exotic electronic structure, well chemical stability, non-toxicity, rich optoelectronic properties, low cost, high surface-to volume ratio and considerable sensitivity at low temperatures, have been regarded as attractive materials for quantum dots sensitized solar cells, lighting emitting components, high frequency devices, and catalysts [17–20]. On the other hand, the above physicochemical characteristics strongly depend on their shape and size, as well as morphology and crystallinity [21, 22].

Besides, nanostructure transformation and crystal growth are very important to fabricate the optoelectronic devices with superior performances [23]. Specifically, nanostructure design strategies offer interesting and extensive ideas to validly synthesize favorable functional nanomaterials due to their distinct characteristics at the nanoscale. For example, ultrafine NiO nanoparticles were acquired in situ by the approach of converting three-dimensional (3D) metal boron organic polymer into one-dimensional (1D) boron organic polymer nanorod array at room temperature [24]. In addition, the facile advance of MgO nanostructures at different annealing temperatures (from 300 to 900 °C) was developed [25]. Moreover, crystal quality is one of the other important factors for optoelectronic devices. Recently, Jang and his coworkers observed the homoepitaxial growth of nanowires with constant outer diameters on bulk materials [26]. Additionally, high performance photodetectors based on p-type $\text{Cu}_{1-x}\text{Ni}_x\text{O}$ films were

prepared, and the crystal quality, morphology, and grain size of $\text{Cu}_{1-x}\text{Ni}_x\text{O}$ films can be manipulated by Ni doping [27]. Of course, crystal growth and its quality are known to be significantly influenced by the crystallization environment.

As a representative n-type semiconductor oxide material with an energy gap of about 3.2 eV, molybdenum oxide (MoO_3) has been extensively used in various devices such as sensors, lithium-ion batteries, and photodetectors due to the high thermal and chemical stability [28–30]. Owing to different experimental conditions, MoO_3 exhibits many nanostructures, for example, nanoribbons, nanosheets, nanowires, nanoflowers and nanorods [29–31]. Consequently, the research regarding MoO_3 nanostructure has gained popularity. However, the morphology transformation induced by annealing temperature is not yet well researched.

Herein, the MoO_3 nanostructure transformation and crystal quality induced by annealing temperature is more compelling. The crystalline MoO_3 was obtained from MoS_2 precursor calcined in the range of 400–900 °C in air, respectively. The results show that the nanostructure can be manipulated from nanoflowers to nanorods via alteration of annealing temperature.

2. Experimental Section

2.1 Materials

Commercially available solvents and metal salts were used without further purification. Specifically, Ammonium molybdate ($(\text{NH}_4)_2\text{MoO}_4$), glucose ($\text{C}_6\text{H}_{12}\text{O}_6$), ammonium fluoride (NH_4F), Thiourea ($\text{CH}_4\text{N}_2\text{S}$), trimethylamine ($\text{C}_6\text{H}_{15}\text{N}$) were purchased commercially from Aladdin company, China.

2.2 Fabrication of MoO_3 materials

The flower-shaped MoS_2 was synthesized by hydrothermal processes similar to our previous study [28]. In a typical synthesis, 1.8 g ammonium molybdate, 1.8 g thiourea, 1 g glucose, firstly, to add 200 mg of ammonium fluoride into 50 mL distilled water, then triethylamine (200 μL) was dropped slowly with a pipette, and stirred vigorously for 30 min. Afterwards, the resulting mixtures were sealed in a 60 mL Teflon-lined stainless-steel autoclave and heated at 200 °C for 24 h, after which the mixtures were cooled to room temperature over 500 min. Thereafter, in the processes of ultrasonication and centrifuging, the obtained MoS_2 suspension was washed several times with absolute ethanol and deionized water to eliminate redundant ions, respectively. The dark flowerlike powders were obtained after dried overnight in vacuum at 80 °C; secondly, the MoS_2 precursor was calcined at 400 °C, 500 °C, 600 °C, 700 °C, 800 °C and 900 °C for 2 h, respectively. All heating rates were set at 1 °C/min. For convenience, the name of the above samples was defined as MoO_3 -400, MoO_3 -500, MoO_3 -600, MoO_3 -700, MoO_3 -800, and MoO_3 -900 according to the calcination temperature, respectively.

On the other hand, the obtained products (MoO_3 -400, MoO_3 -500, MoO_3 -600, MoO_3 -700, MoO_3 -800, and MoO_3 -900) were grinded thoroughly in an agate mortar to form a gas-sensing paste, respectively. Then, the paste was uniformly coated on the alumina ceramic tube in turn, and annealed in air at 120 °C for 2 h. Here, the gas response magnitude of the sensor is defined as $S = R_a/R_g$, where R_a and R_g are the resistance in air and in the detected gas, respectively. Additionally, the response time and the recovery time were expected to be the minimum time required for the gas sensor output to reach 90% of its saturation after the gas was applied or shut off from the chamber.

2.3 Characterizations

The morphology of the products was investigated by a field emission scanning electron microscope (FESEM, Zeiss Gemini 500). The microstructure of the samples was investigated using X-ray diffraction (XRD, Rigaku Smartlab). X-ray photoelectron spectroscopy (XPS, Termo Scientific Escalab 250xi) was measured to further confirm the surface element composition and chemical state. And the Gas sensing properties were measured by the gas sensing system of MA1.0 (Narui Electronics Co. Ltd., China).

3. Result And Discussion

Figure 1 shows the typical FESEM images of the as-prepared MoO_3 samples. Specifically, hierarchical flower-like samples were observed by high resolution SEM images of Fig. 1 a-c, which are the samples of MoO_3 -400, MoO_3 -500, and MoO_3 -600, respectively. As a whole, the profile of the three samples are almost same, the microspheres, which the average diameter is less than 1 μm , are constructed by numerous plate-like nanosheets, and the edge thicknesses are about 19 nm. These irregular nanospheres are interconnected each other, facilitating electron transport and ethanol diffusion. After annealing, the hierarchical flower-like morphology was vanished. On the contrary, a lot of nanosheets were synthesized with increased thickness. Interestingly, the nanosheet thickness of sample MoO_3 -600 become larger than that of MoO_3 -400 and MoO_3 -500, due to the growth of the MoO_3 crystalline grain at high temperature. In addition, it can be clearly observed that the voids enclosed by numerous primary ultrathin nanosheets with clear texture. Concretely, the diameter of nanoflowers derived from MoO_3 calcined in 400 °C is about 0.3 μm , the sample calcined in 500 °C is about 0.5 μm , the sample calcined in 600 °C is about 4 μm . Figure 1d-f show the nanostructures of MoO_3 annealed between 700 and 900 °C. Compared with the samples annealed at lower temperature, the MoO_3 annealed between 700 and 900 °C exhibit the morphology of nanosheets, which represent higher crystallization. What's more, the thickness of nanosheets is rising with the increase of annealing temperature. The thickness of nanosheets derived from the sample annealed at 700 °C is 0.031 μm , the sample annealed at 800 °C is 0.145 μm , and the sample annealed at 900 °C is 1.690 μm . In terms of crystal growth, almost every point on the unpolished surface of a crystal can be filled with atoms to become the point where the crystal grows. The nanoflowers we obtained above, which has rougher surface than nanosheets, each point on the surface can be filled by atoms so as to becoming smooth and flush through supplying energy by calcining in high temperature. Certainly, as for the smooth surfaces, their consistent growth needs to be thermally

activated [32]. Consequently, the samples obtained with 700–900 °C can grow thicker with the annealing temperature increasing due to the more power and thermal provided.

To the best of our knowledge, the crystallinity, electronic structure and phase stability were strongly influenced by the calcination temperature and composition of the metal oxide semiconductor materials, especially the nanocomposites. Figure 2a shows the XRD patterns of MoO₃ samples which were calcined at different temperature. Evidently, the diffraction peaks of all the samples are consistent with the orthorhombic MoO₃ (JCPDS 05-0508). The intensity peaks at $2\theta = 12.8, 25.7, \text{ and } 39.1$ corresponding to (020), (110), (040), (021), and (060) planes, respectively. This indicates that the sample grows with intense preferential orientation of (110). No other diffraction peaks are observed, which confirm that MoO₃ samples with relatively high crystal purity. Interestingly, the peak intensity increases with the annealing temperature from 400 to 900 °C, which attributes to the good crystalline at high calcined temperature. On the other hand, the intensities of the peaks were gradually increased with the increase of annealing temperature. It indicates that the crystallinity of the samples was significantly improved via increasing annealing temperature. For example, the intensity of the peak (040) of MoO₃-900 is more than three times as compared with that of MoO₃-400.

On the basis of the above analysis, the chemical ingredient and the valence state of the elements in the MoO₃-600 nanosheets were analyzed via XPS. The corresponding results are shown in Fig. 2b and c. The Mo spectrum in Fig. 2b displays two ?? peaks located at 232.7 and 235.8 eV, ascribe to Mo 3d_{5/2} and Mo 3d_{3/2}, respectively, indicating that the chemical state of Mo element is present as Mo⁶⁺ in MoO₃-600. Further, the energy separation of two peaks is 3.2 eV, which indicates the successful fabrication of MoO₃ [30]. The peak of O 1s can be deconvoluted into two independent oxygen species at 529.8 and 531.4 eV (Fig. 2c). The peak at 529.8 eV in the O 1s curve can be attributed to the oxygen ions in the crystal lattice that is lattice oxygen O_{lattice} (O²⁻) and surface adsorbed oxygen O_{ads}. (e.g., O⁻) [33]. While the other peak at 531.4 eV were assigned to the oxygen ions species such as O⁻, O²⁻, and O₂⁻. Compared to the lattice oxygen, the absorbed O_x⁻ are active to ethanol, so they play a key role in enhancing the sensing performance [34, 35].

In order to investigate the optimum working temperature of different MoO₃ samples annealed at various temperature from 50 to 350 °C to 10 ppm of ethanol, as shown in Fig. 3. Evidently, all the sensor's response increase firstly before 200 °C, and then decrease drastically with the increase of operation temperature further. Among them, the MoO₃-600 sensor exhibits the maximum response of 8.06 towards 100 ppm ethanol at 200 °C, which is three times higher than those of MoO₃-400 and MoO₃-900, respectively. Compared with the MoO₃-600, the response values of MoO₃-400, MoO₃-500, MoO₃-700, MoO₃-800 and MoO₃-900 are 3.18, 5.34, 5.81 and 4.50 at 200 °C, respectively. All in all, among all the sensors, the response of MoO₃-600 based sensor increases faster than that of others devices such as MoO₃-400, MoO₃-500, MoO₃-700, MoO₃-800 and MoO₃-900. These demonstrate that the nanostructure and annealing temperature of MoO₃ have a considerable effect on the device's response, and inclination

of response increases significantly and then gradually decreases. A suitable working temperature is indispensable in that ample thermal energy is a necessary prerequisite to overcome the chemical barrier of gas and the activation barrier of surface reaction. Besides, when the working temperature is further increased, the gas desorption rate is higher than adsorption rate, which is unfavorable to the response.

Figure 4a gives the dynamic response and recovery characteristics of the MoO₃-600 based sensor to different alcohol concentrations from 5 to 500 ppm CH₃CH₂OH at 200 °C. Obviously, as the ethanol concentration increases, the response of the MoO₃-600 sensor climbs continually, thereafter, the response approaches the saturation value when the CH₃CH₂OH concentration overpass 500 ppm, see Fig. 4b. The similar results have been reported by other literature [35, 36]. It can be explained that more ethanol molecules can be physically or chemically adsorbed on the MoO₃-600 nanosheets, and speeding up the surface reaction rate with the chemisorbed oxygen species such as O⁻ and O₂⁻ [30, 36]. Additionally, according to the sensing mechanism of MoO₃, the increase of crystallization has an irreplaceable influence on its sensing properties [30, 36]. On the other hand, the limit of detection (LoD) of ethanol was evaluated by the method of linear extrapolation, specifically, the response sensitivity is a function of ethanol concentration (the inset of Fig. 4b). The detailed calculating formula of the LoD is: LoD = 3 × (Standard Deviation/Slope), from which the ultra-low ethanol detection concentration is 125 ppb for the MoO₃ sensor. Figure 4c shows a typical repeatability performance of the MoO₃ based sensor toward 100 ppm ethanol at 200 °C, which exhibits its superb stability and repeatability. Moreover, the response time (τ_{res}) and recovery time (τ_{recov}) are examined and the results indicate that the MoO₃-600 sensor exhibits a very quick response and recovery properties to ethanol (Fig. 4d). Figure 4d gives the τ_{res} and τ_{recov} of the MoO₃-600 sensor toward 100 ppm ethanol, which are 7 s and 26 s, respectively.

From the aspect of practical applications, selectivity is another very important characteristics of the gas sensor. Herein, the sensing properties of MoO₃ nanosheets sensor to other various VOCs, for example, benzene, isopropanol, chloroform, acetic acid, methanol and acetone were evaluated. The selective property of the MoO₃-600 sensor towards 100 ppm of the above gas at 200 °C is shown in Fig. 5a. Clearly, the maximum gas response value of MoO₃ toward 100 ppm alcohol is 8.06, which is evidently larger than those of other gases. Specifically, the responses to benzene, isopropanol, chloroform, acetic acid, methanol and acetone are 0.23, 1.47, 1.47, 1.57, 1.74 and 2.31, respectively. Therefore, the sensitivity of the MoO₃-600 towards ethanol is much higher than that of other VOCs, indicating that it has an excellent selectivity to ethanol.

The sensing mechanism of the MoO₃-600 to ethanol can be illustrated by surface conduction modulation model. According to the literature [16, 22], the adsorption and desorption of target gas molecules from the surface of the MoO₃-600 could regulate the electrical resistance of gas sensor. When the MoO₃-600 is exposed to fresh air, the oxygen molecules (O₂) will capture conductive band electrons (e^{-1}) to form chemisorbed oxygen ions species (O⁻ and O₂⁻). This process will form a depletion layer on its surface region of sensing material, which causes the device resistance increase. When the MoO₃-600 sensor was

exposed to ethanol gas, the ethanol molecules can react with the oxygen species O^- and O_2^- , resulting in the release of trapped electrons back to the conduction band, thereby significantly reducing the sensor resistance. This reaction processes can be expressed as Equations (1) and (2) [37, 38]:



4. Conclusion

In conclusion, various MoO_3 nanomaterials were successfully prepared by hydrothermal and calcined processes. The nanostructure morphology and crystal quality of MoO_3 have temperature-depend relationships. According to the results, the MoO_3 morphology can be manipulated by annealing temperature from nanoflowers, nanosheets to nanorods. In addition, the ethanol sensing performances were carefully investigated by MoO_3 samples. It is found that the MoO_3 -600 has an excellent sensing performance duo to the combination of degree of crystallinity and nanostructure.

Declarations

Acknowledgements

This work was financially supporting from the National Natural Science Foundation of China (Grant No. 51227804). Projects of Science and Technology Commission of Shanghai Municipality Grant Nos. (19ZR1473800, 14DZ2260800). This work was also funded by the Postdoctoral Scientific Research Foundation of Qingdao. National College Students Innovation and Entrepreneurship Training Program of China (No. G201811065023). The authors would like to thank the Chemical Experimental Teaching Center of Qingdao University for the Measurement Support, and Kehui Han from Shiyanjia Lab (www.shiyanjia.com) for the XRD analysis.

Conflict of interest

The authors declare that they have no competing financial interest.

References

1. X. Gao, T. Zhang, An overview: Facet-dependent metal oxide semiconductor gas sensors. *Sensor Actuat B-chem* **277**, 604–633 (2018)

2. Z. Wang, P. Nayak, A. Jesus, H. Alshareef, Recent Developments in p-Type Oxide Semiconductor Materials and Devices. *Adv Mater* **28**, 3831–3892 (2016)
3. X. Qian, X. Liu, B. Wan, Z. Yang, F. Li, J. Lu, G. Hu, C. Pan, Z. Wang, In₂O₃ Nanowire Field-Effect Transistors with Sub-60 mV/dec Subthreshold Swing Stemming from Negative Capacitance and Their Logic Applications. *ACS Nano* **12**, 9608–9616 (2018)
4. S. Li, Y. Zhang, W. Yang, H. Liu, X. Fang, 2D perovskite Sr₂Nb₃O₁₀ for high-performance UV photodetectors. *Adv Mater* **32**, 1905443 (2020)
5. Y. Zhang, X. Zhao, J. Chen, S. Li, W. Yang, X. Fang, Self-polarized BaTiO₃ for greatly enhanced performance of ZnO UV photodetector by regulating the distribution of electron concentration. *Adv. Funct. Mater.* **30**, 1907650 (2020)
6. J. Niu, C. Zeng, H. Peng, X. Lin, P. Sathishkumar, Y. Cai, Formation of N-Doped Carbon-Coated ZnO/ZnCo₂O₄/ CuCo₂O₄ Derived from a Polymetallic Metal–Organic Framework: Toward High-Rate and Long-Cycle-Life Lithium Storage. *Small* **13**(47), 1702150 (2017)
7. C. Zhao, D. Zhong, D. Zhong, L. Liu, Y. Yang, H. Shi, L. Peng, Z. Zhang, Strengthened Complementary Metal–Oxide–Semiconductor Logic for Small-Band-Gap Semiconductor-Based High-Performance and Low-Power Application. *ACS Nano* **14**(11), 15267–15275 (2020)
8. C. Su, L. Zhang, Y. Han, C. Ren, M. Zeng, Z. Zhou, Y. Su, N. Hu, H. Wei, Z. Yang, Controllable synthesis of heterostructured CuO–NiO nanotubes and their synergistic effect for glycol gas sensing. *Sensor Actuat B-chem* **304**, 127347 (2020)
9. S. Fields, S. Smith, P. Ryan, S. Jaszewski, I. Brummel, A. Salanova, G. Esteves, S. Wolfley, M. Henry, P. Davids, J. Ihlefeld, Phase-Exchange-Driven Wake-Up and Fatigue in Ferroelectric Hafnium Zirconium Oxide Films. *ACS Appl Mater Inter* **12**, 26577–26585 (2020)
10. Z. Long, X. Xu, W. Yang, M. Hu, D. Shtansky, D. Golberg, X. Fang, Cross-bar SnO₂-NiO nanofiber-arrays-based transparent photodetectors with high detectivity. *Adv Electron Mater* **6**, 1901048 (2020)
11. A. Bathinapatla, S. Kanchi, M. Sabela, Y. Ling, K. Bisetty, Inamuddin, Experimental and Computational Studies of a Laccase Immobilized ZnONPs/GO-Based Electrochemical Enzymatic Biosensor for the Detection of Sucralose in Food Samples. *Food Anal Method* **13**, 2014–2027 (2020)
12. T. Inamuddin, Rangreez, A. Asiri, Fabrication and optimization of Cu(II) ion selective membrane electrode. *J Water Chem Techno* **39**, 220–227 (2020)
13. S. Shen, X. Zhang, X. Cheng, Y. Xu, S. Gao, H. Zhao, X. Zhou, L. Huo, Oxygen-Vacancy-Enriched Porous α-MoO₃ Nanosheets for Trimethylamine Sensing. *ACS Appl Nano Mater* **2**, 8016–8026 (2019)
14. S. Zhou, Q. Lu, M. Chen, H. Bo Li, Wei, B. Zi, J. Zeng, Y. Zhang, J. Zhang, Z. Zhu, Q. Liu, Platinum-Supported Cerium-Doped Indium Oxide for Highly Sensitive Triethylamine Gas Sensing with Good Antihumidity. *ACS Appl Mater Inter* **12**(38), 42962–42970 (2020)
15. L. Zheng, F. Teng, X. Ye, H. Zheng, X. Fang, Photo/electrochemical applications of metal sulfide/TiO₂ heterostructures. *Adv Energy Mater* **10**, 1902355 (2020)

16. P. Wang, S. Wang, Y. Kang, Z. Sun, X. Wang, Y. Meng, M. Hong, W. Xie, Cauliflower-shaped Bi₂O₃/ZnO heterojunction with superior sensing performance towards ethanol. *J. Alloy. Compd.* **854**, 157152 (2021)
17. N. Graddage, J. Ouyang, J. Lu, T. Chu, Y. Zhang, Z. Li, X. Wu, P. Malenfant, Y. Tao, Near-Infrared-II Photodetectors Based on Silver Selenide Quantum Dots on Mesoporous TiO₂ Scaffolds. *ACS Appl Mater Inter* (2020). <https://dx.doi.org/10.1021/acsanm.0c02686>
18. X. Zhuang, S. Patel, C. Zhang, B. Wang, Y. Chen, H. Liu, V. Dravid, J. Yu, Y. Hu, W. Huang, A. Facchetti, T. Marks, Frequency-Agile Low-Temperature Solution-Processed Alumina Dielectrics for Inorganic and Organic Electronics Enhanced by Fluoride Doping. *J. Am. Chem. Soc.* **142**(28), 12440–12452 (2020)
19. R. Medhi, M. Marquez, T. Lee, Visible-Light-Active Doped Metal Oxide Nanoparticles: Review of their Synthesis, Properties, and Applications. *ACS Appl Nano Mater* **3**, 6156–6185 (2020)
20. Q. Qian, Y. Li, Y. Liu, L. Yu, G. Zhang, Ambient Fast Synthesis and Active Sites Deciphering of Hierarchical Foam-Like Trimetal–Organic Framework Nanostructures as a Platform for Highly Efficient Oxygen Evolution Electrocatalysis. *Adv Mater* **31**(23), 1901139 (2019)
21. T. Zhang, B. Huang, A. Elzatahry, A. Alghamdi, Q. Yue, Y. Deng, Synthesis of Podlike Magnetic Mesoporous Silica Nanochains for Use as Enzyme Support and Nanostirrer in Biocatalysis. *ACS Appl Mater Inter* **12**, 17901–17908 (2020)
22. M. Lei, X. Zhou, Y. Zou, J. Ma, F. Alharthi, A. Alghamdi, X. Yang, Y. Deng, A facile construction of heterostructured ZnO/Co₃O₄ mesoporous spheres and superior acetone sensing performance. *Chin Chem Lett* (2020). <https://doi.org/10.1016/j.ccllet.2020.10.041>
23. Y. Ren, Y. Zou, Y. Liu, X. Zhou, J. Ma, D. Zhao, G. Wei, Y. Ai, S. Xi, Y. Deng, Synthesis of orthogonally assembled 3D cross-stacked metal oxide semiconducting nanowires. *Nat. Mater.* **19**(2), 203–211 (2020)
24. X. Zhao, C. Xiang, F. Zhang, F. Yao, R. Sheng, Q. Ding, W. Liu, H. Zhang, X. Zhou, Transformation from 3D Boron Organic Polymers to 1D Nanorod Arrays: Loading Highly Dispersed Nanometal for Green Catalysis. *ACS Appl Mater Inter* **11**(46), 43214–43222 (2019)
25. N. Rani, S. Chahal, P. Kumar, A. Kumar, R. Shukla, S. Singh, MgO nanostructures at different annealing temperatures for d(0) ferromagnetism. *Vacuum* **179**, 109539 (2020)
26. J. Hyunseok, Z. Chao, K. Xiao, S. Jaejung, D. Feng, C. Seungho, Homoepitaxial growth of ZnO nanostructures from bulk ZnO. *J Colloid Interf Sci* (2020). <https://doi.org/10.1016/j.jcis.2020.10.078>
27. W. Yin, J. Yang, K. Zhao, High Responsivity and External Quantum Efficiency Photodetectors Based on Solution-Processed Ni-Doped CuO Films. *ACS Appl Mater Inter* **12**(10), 11797–11805 (2020)
28. F. Zhang, Y. Wang, L. Wang, J. Liu, H. Ge, B. Wang, X. Huang, X. Wang, Z. Chi, W. Xie, High performance In₂(MoO₄)₃@In₂O₃ nanocomposites gas sensor with long-term stability. *J. Alloy. Compd.* **805**, 180–188 (2019)

29. L. Zhua, W. Zenga, Y. Lib, J. Yanga, Enhanced ethanol gas-sensing property based on hollow MoO₃ microcages. *Physica E* **106**, 170–175 (2019)
30. Z. Tanga, X. Denga, Y. Zhanga, X. Guod, J. Yanga, C. Zhua, J. Fana, Y. Shia, B. Qinga, F. Fan, MoO₃ nanoflakes coupled reduced graphene oxide with enhanced ethanol sensing performance and mechanism. *Sensor Actuat B-chem* **297**, 126730 (2019)
31. J. Hu, X. Wang, M. Zhang, Y. Sun, P. Li, W. Zhang, K. Lian, L. Chen, Y. Chen, Synthesis and characterization of flower-like MoO₃/In₂O₃ microstructures for highly sensitive ethanol detection. *RSC Adv* **7**, 23478 (2017)
32. W. Xie, Z. Pang, Y. Zhao, F. Jiang, H. Yuan, H. Song, S. Han, Structural and optical properties of ε-phase tris(8-hydroxyquinoline) aluminum crystals prepared by using physical vapor deposition method. *J. Cryst. Growth* **404**, 164–167 (2014)
33. X. Chen, S. Wang, C. Su, Y. Han, C. Zou, M. Zeng, N. Hu, Y. Su, Z. Zhou, Z. Yang, Two-dimensional Cd-doped porous Co₃O₄ nanosheets for enhanced room temperature NO₂ sensing performance. *Sensor Actuat B-chem* **305**, 127393 (2020)
34. D. Wang, Y. Yin, P. Xu, F. Wang, P. Wang, J. Xu, X. Wang, X. Li, Catalytic-induced Sensing Effect of Triangular CeO₂ Nanoflakes for Enhanced BTEX Vapor Detection with Conventional ZnO Gas Sensors. *J Mater Chem A* **8**, 11188–11194 (2020)
35. D. Wang, L. Deng, H. Cai, J. Yang, L. Bao, Y. Zhu, X. Wang, Bimetallic PtCu Nanocrystal Sensitization WO₃ Hollow Spheres for Highly Efficient 3-hydroxy-2-butanone Biomarker Detection. *ACS Appl Mater Inter* **12**(16), 18904–18912 (2020)
36. X. Huang, Z. Chi, J. Liu, D. Li, X. Sun, C. Yan, Y. Wang, H. Li, X. Wang, W. Xie, Enhanced gas sensing performance based on p-NiS/n-In₂O₃ heterojunction nanocomposites. *Sens. Actuators B* **304**, 127305 (2020)
37. K. Zhang, S. Qin, P. Tang, Y. Feng, D. Li, Ultra-sensitive ethanol gas sensors based on nanosheet-assembled hierarchical ZnO-In₂O₃ heterostructures. *J. Hazard. Mater.* **391**, 122191 (2020)
38. D. Zhang, Y. Cao, J. Wu, X. Zhang, Tungsten trioxide nanoparticles decorated tungsten disulfide nanoheterojunction for highly sensitive ethanol gas sensing application. *Appl Surf Sci* **503**, 144063 (2020)

Figures

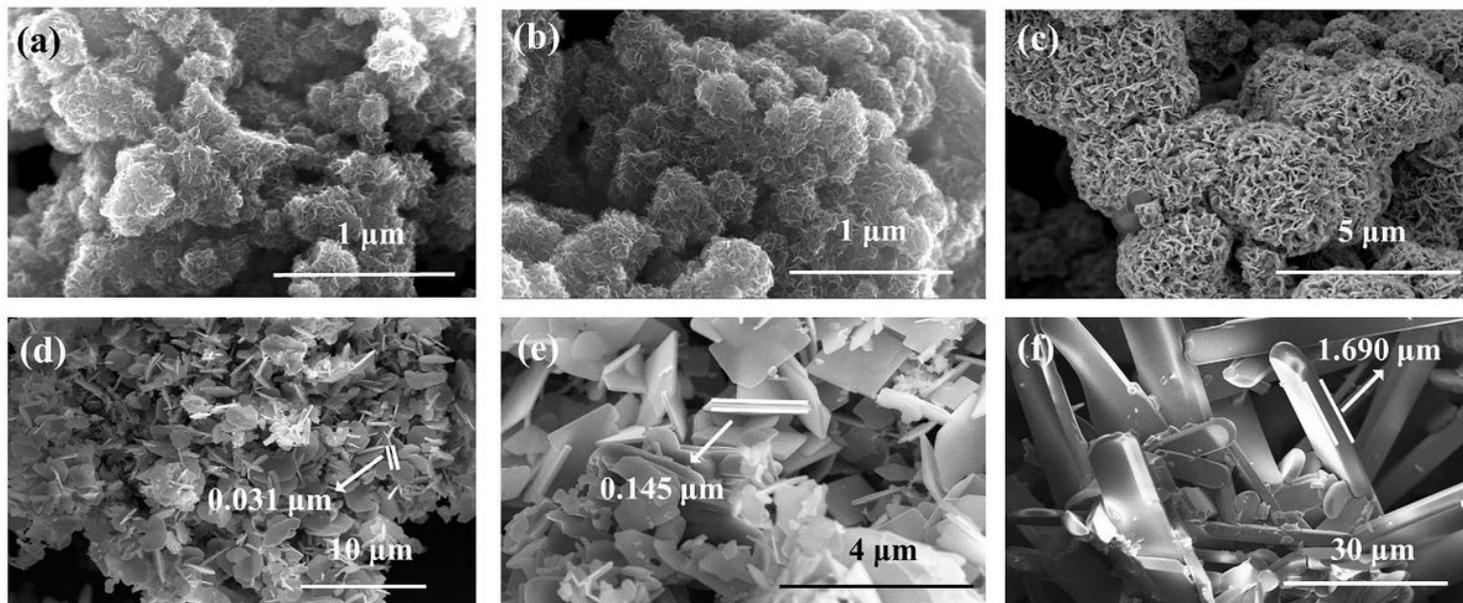


Figure 1

Typical FESEM images of MoO₃. (a) to (f) are the samples of MoO₃-400, MoO₃-500, MoO₃-600, MoO₃-700, MoO₃-800, and MoO₃-900, respectively.

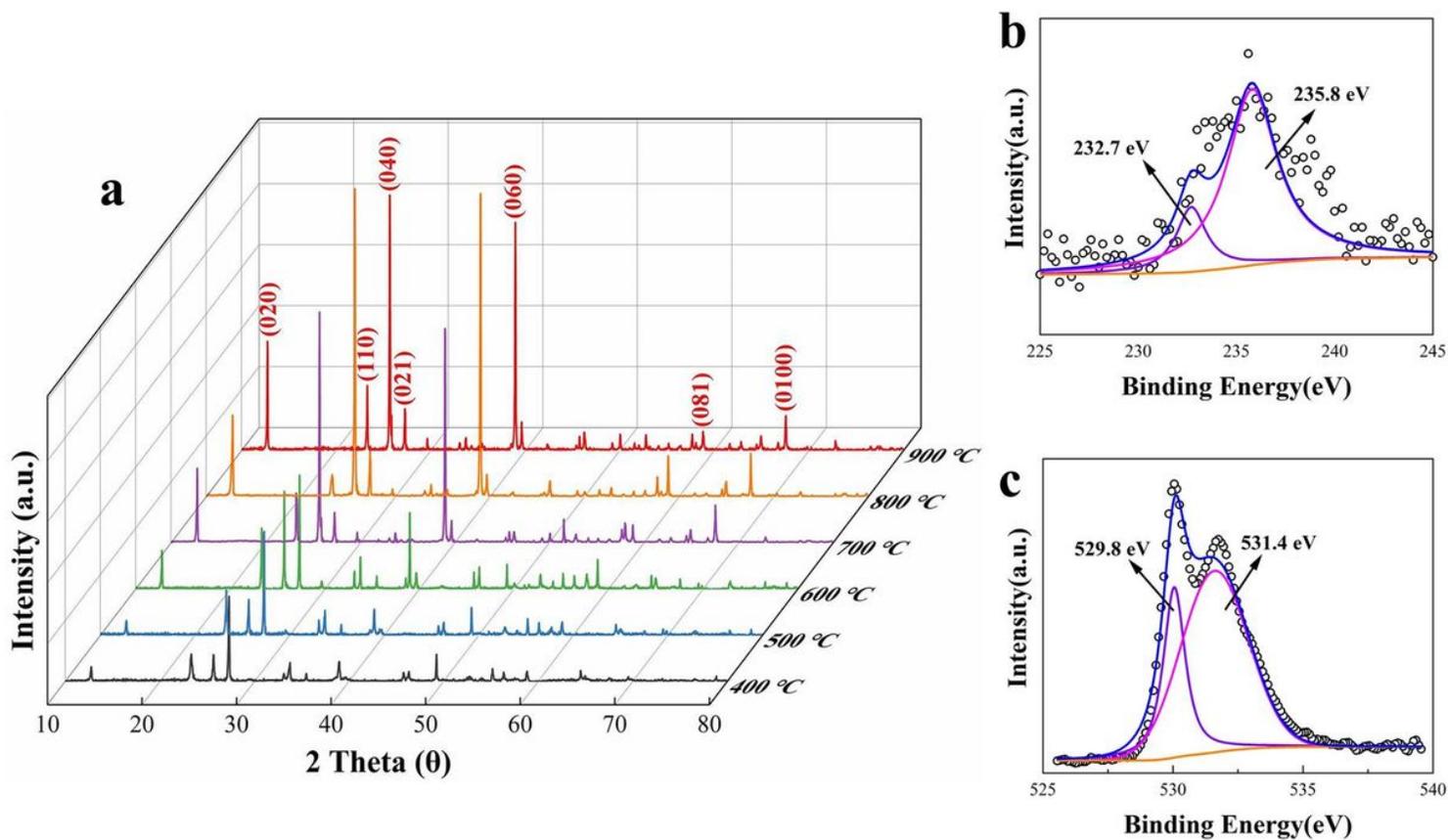


Figure 2

The X-ray diffraction pattern (a) and XPS spectra of Mo (b) and O (c).

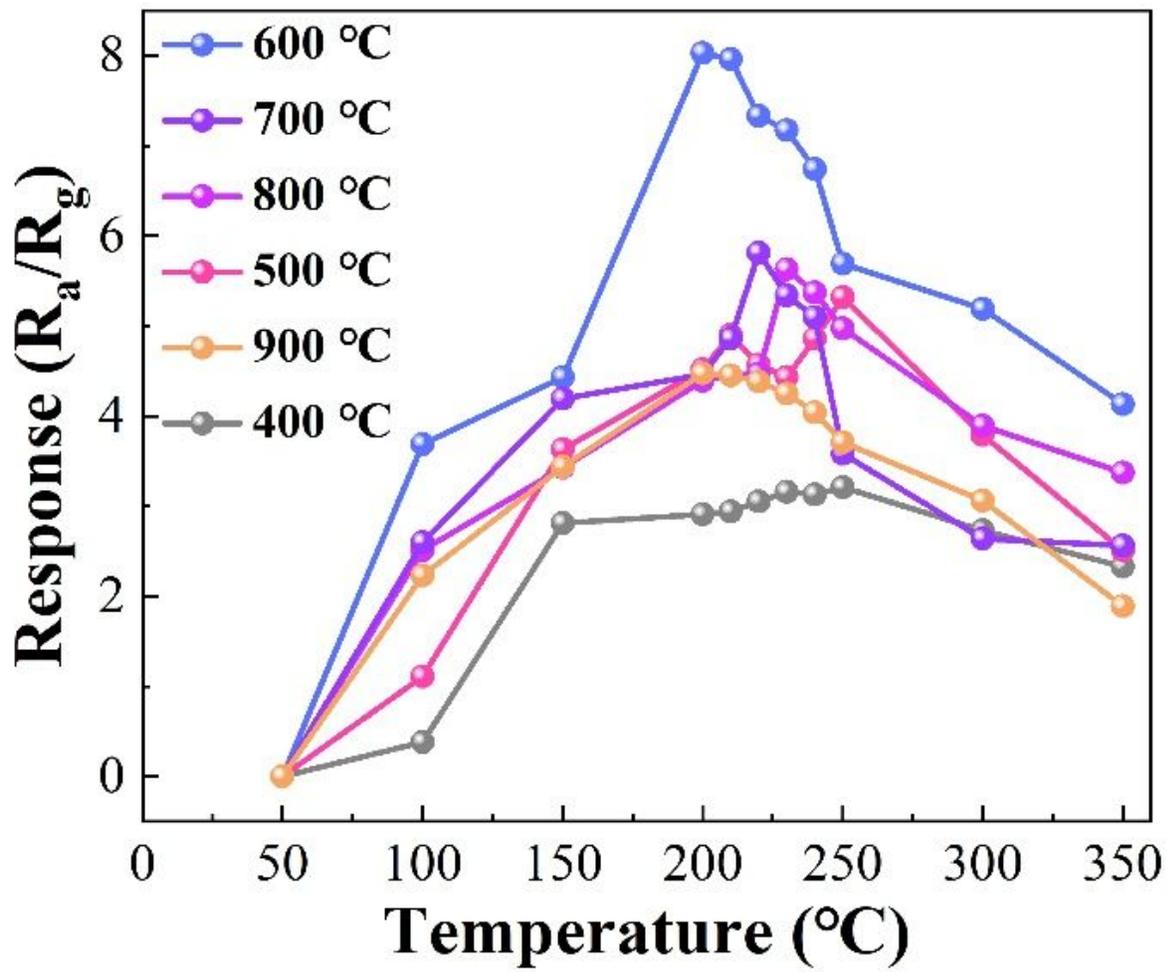


Figure 3

Responses of different MoO₃ samples to 100 ppm ethanol gas.

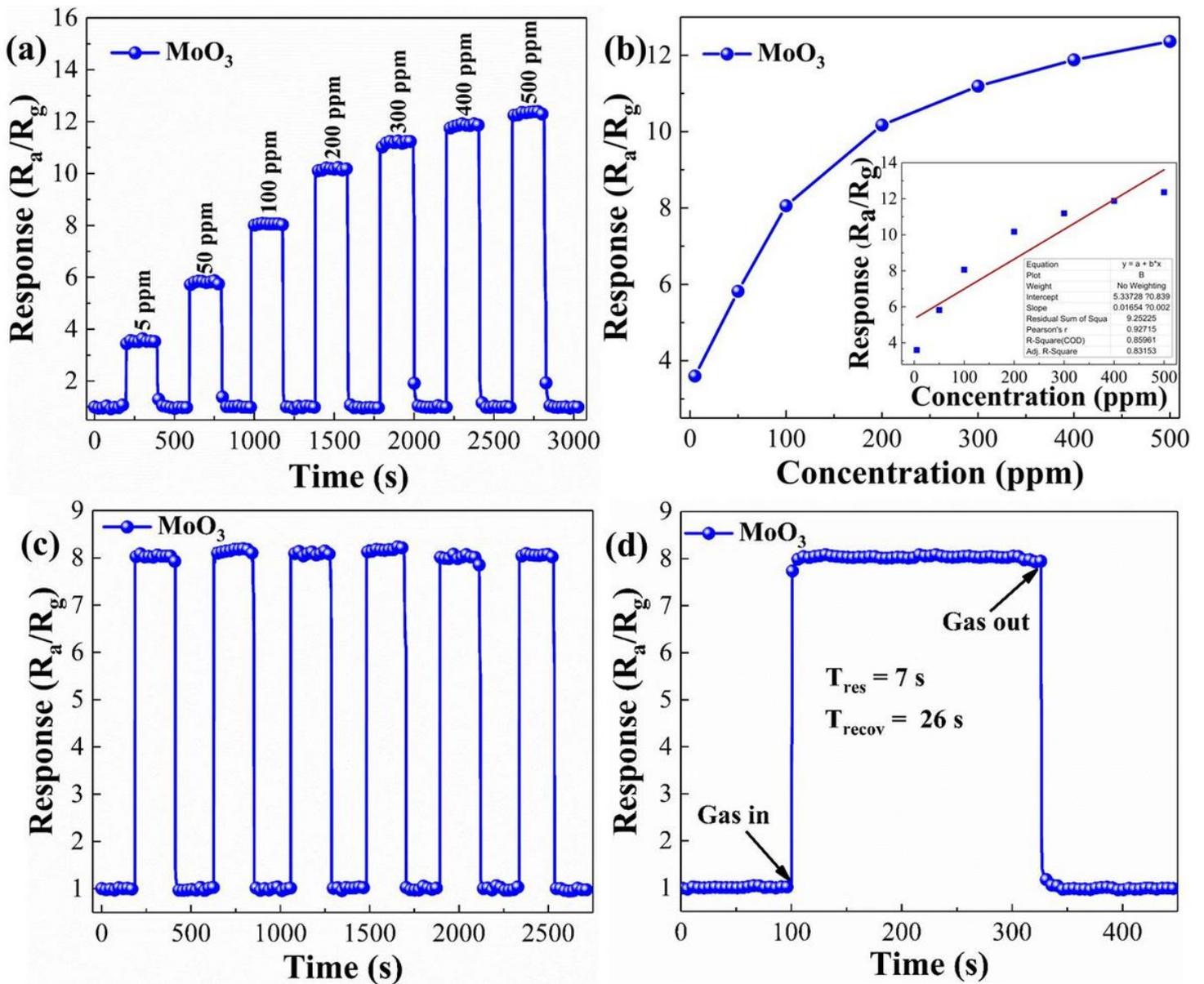


Figure 4

(a) The responses of the MoO₃-600 sensor to different concentrations ethanol from 5 ppm to 500 ppm at 200 °C; (b) The curve of response and gas concentration for MoO₃-600 sensor, and the inset is the calculated LoD of MoO₃-600; (c) The response repeatability test of the gas sensor to 100 ppm ethanol at 200 °C; (d) The response/recovery time curves of the MoO₃-600 sensor toward 100 ppm ethanol at 200 °C.

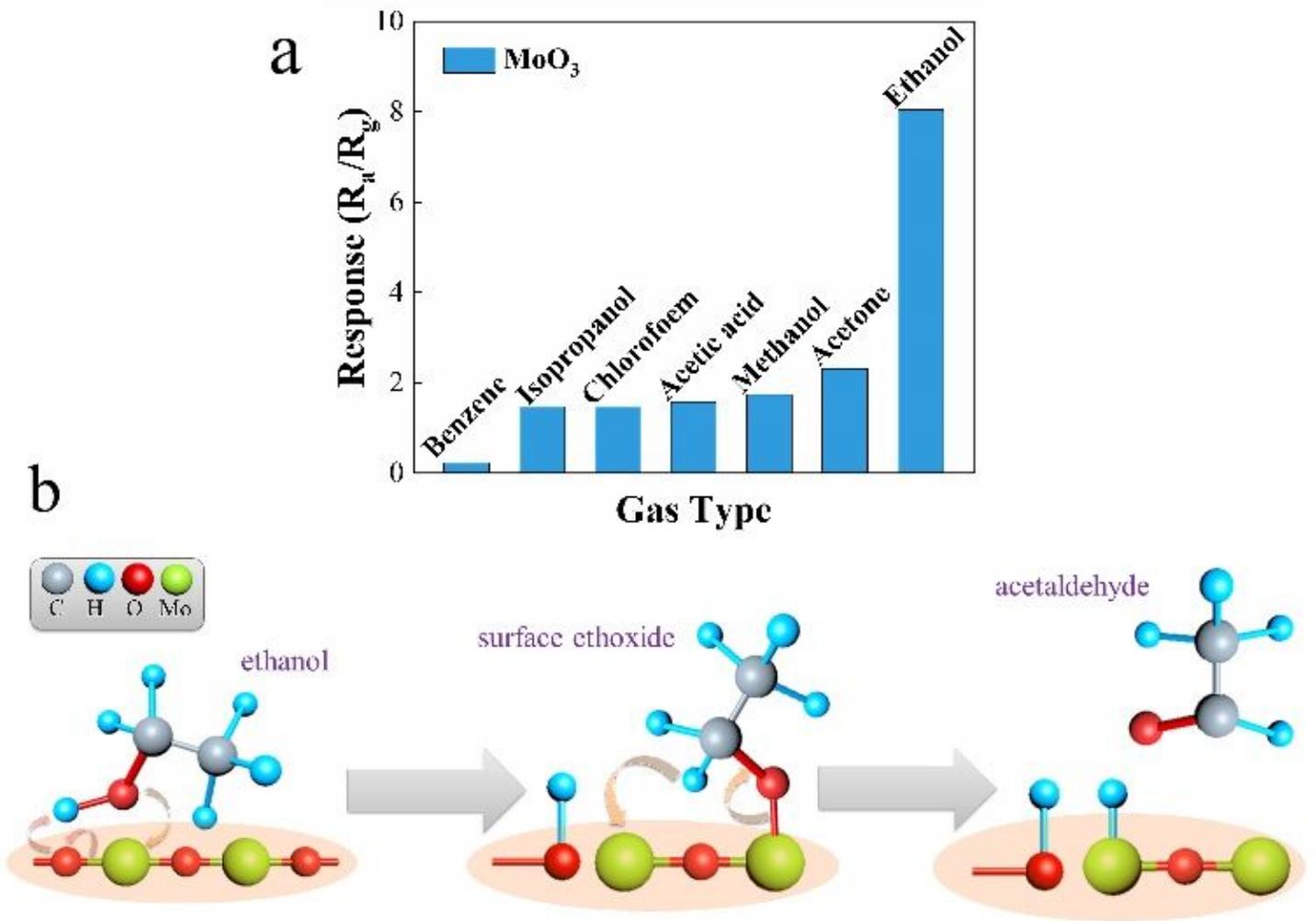


Figure 5

(a) The selectivity of the MoO₃-600 sensor to different VOC gases with a concentration of 100 ppm at 200 °C; (b) The schematic of sensing mechanism of MoO₃-600.